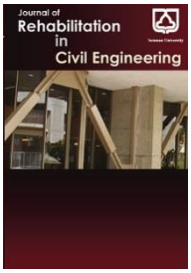

Journal homepage: http://civiljournal.semnan.ac.ir/

A Modeling Strategy for Predicting the Response of Steel Plate-Concrete Composite Walls

Mohammad Sadegh Barkhordari[1*]
1. PhD, Department of Civil & Environmental Engineering, Amirkabir University of Technology (Tehran Polytechnic), Tehran, Iran.
Corresponding author: *m.s.barkhordari@aut.ac.ir*

ARTICLE INFO

Article history:
Received: 30 March 2022
Revised: 26 June 2022
Accepted: 27 June 2022

Keywords:
Steel-plate composite shear wall;
Smeared crack model;
Semi-macro model;
Cyclic loading;
Steel faceplate.

ABSTRACT

Shear walls are among lateral load resisting systems which are used to provide adequate stiffness, strength, and nonlinear deformation capacity to withstand strong ground motion. Usually at the base of the wall, these structures tolerate inelastic deformations subjected to strong ground motions. Researchers have offered composite walls to solve these problems. Steel plate-concrete composite (SCC) walls have been regarded as an alternative to reinforced concrete walls in terms of seismic performance and constructability. In this study, a new semi-macro modified fixed strut angle finite element model is proposed to predict the nonlinear response of SCC walls using OpenSees. A new modified fixed strut angle model and a quadrilateral flat shell element are adapted to the analysis of SCC shear walls. The numerical model is validated using the results of a set of experimental data reported in the literature. Comprehensive comparisons between analytical-model-predictions and experimental data suggest that the numerical model can accurately simulate the steel plate-concrete composite wall responses.

1. Introduction

Reinforced concrete members have been used for several reasons [1,2] including, but not limited to, large lateral stiffness and nonlinear deformation capacity. Usually at the base of the wall, these structures tolerate inelastic deformations subjected to strong ground motions [3]. Some seismic codes determine a limit for the axial load ratio and the transverse reinforcement amount [4]. The wall's reinforcement ratio and thickness are often increased to ensure that the lower shear wall of high-rise buildings can meet codes requirements [2,6]. Thicker concrete walls not only occupy much utilizable floor space, but also increase the total weight of the structure and accordingly amplify seismic forces [7]. In addition, the dense

How to cite this article:
Barkhordari, M. S. (2023). A Modeling Strategy for Predicting the Response of Steel Plate-Concrete Composite Walls. Journal of Rehabilitation in Civil Engineering, 11(2), 43-63.
https://doi.org/ 10.22075/JRCE.2022.26725.1632

reinforcement can cause serious difficulties in construction. Researchers have offered composite walls to solve these problems. These composite structural members can be classified into three categories including steel reinforced concrete (SRC) walls, steel frame boundary and infilled RC walls, and steel panels combined with concrete walls (steel-plate concrete composite (SCC) or the single/double skin composite wall [8]– Fig. 1). SC walls comprise a concrete core reinforced with steel faceplates on both surfaces. SC walls have demonstrated constructability and seismic performance under mechanical loading. Laboratory studies and FEM analysis were performed by Ozaki et al. [9] to investigate the behavior of steel-plate reinforced concrete panels. The results showed that the web openings had no impact on the shear strain of the steel-plate reinforced concrete panels at the onset of steel faceplate yielding and concrete cracking. Vecchio and McQuade [10] investigated the behavior of SCC shear walls using a smeared rotating crack model. The numerical model was developed using VecTor2 [11].

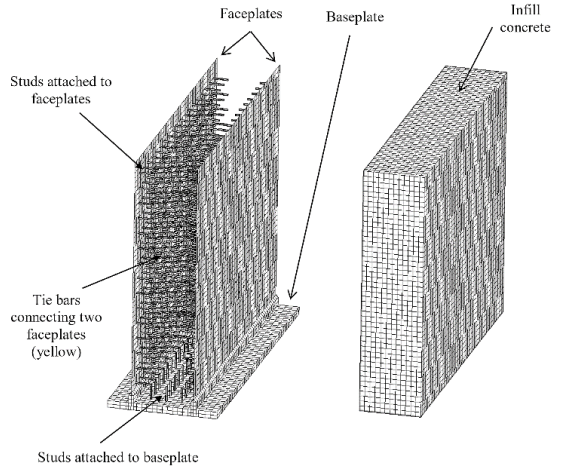

Fig 1. SCC shear wall [8,12].

Numerical model validation studies were then performed by modeling various test specimens and comparing laboratory and numerical results. The defect reported by them was modeling the Buckling of steel faceplate element and its effects on the response. Also, 2D nonlinear finite element analysis algorithm remarkably overestimated the stiffness. Xiaowei et al. [13] investigated the behavior of SCC shear walls using the general FE package MSC.Marc. One of the important parameters examined was the slippage characteristic of the steel plate-concrete interface. They used the spring elements to investigate the slip effect between the steel faceplates and the infill concrete. However, pinching and stiffness as well as strength deteriorations were not considered. Xiaowei et al. [13] proposed the axial force-moment interaction curves for SCC shear walls using the results of the parametric study. Rafiei et al. [14] investigated the behavior of SC shear walls under in-plane load using ABAQUS software. They developed two different finite element models to investigate the behavior of the steel plate-concrete interface. The design parameters which were studied were (a) the fasteners configuration, (b) compressive strength of the concrete, and (c) yield strength of the steel plate. Ali et al. [15] used ABAQUS software to predict the behavior of flanged SC walls. The backbone curve obtained using ABAQUS was consistent with the results of the cyclic loading test of four SC walls. The finite element (FE) models did not capture the pinching behavior seen in the experiments. Varma et al. [16,17] proposed a simplified model to simulate the in-plane response of SC panels under shear forces using a smeared crack model and a multi-axial plasticity with Von-Mises yield surface to simulate the behavior of the concrete and the steel faceplates, respectively. Kurt et al. [18] used LS-DYNA to develop and validate FE models for modeling the steel-plate concrete

composite shear walls under in-plane cyclic loading and their anchorage to the concrete basemat. The effects of shear connector design and composite action of the SC walls were investigated by Zhang et al. [19] using ABAQUS. Nonlinear finite element analyses were used to expand the experimental database. They provided the design criteria (for connector spacing) implemented in AISC N690s1 [20]. Epackachi et al. [8] conducted numerical modeling to study the cyclic response of the SCC shear walls. A nonlinear finite element model was developed in LS-DYNA. The validated DYNA model was used to investigate the effect of interface friction between the infill concrete and the steel faceplates, and the shear studs distribution. In a similar study conducted by Nguyen and Whittaker [21] it was shown that ABAQUS models of SCC shear walls can be developed to simulate the in-plane response and study key design variables such as a faceplate slenderness ratio, connector type, and reinforcement ratio. Wang et al. [22] tested and simulated corrugated steel plate concrete composite shear walls (SPCSWs) by ABAQUS to investigate the seismic performance of the corrugated SPCSWs. They corrugated SPCSW showed good ductility, high-bearing capacity, high energy dissipation capacity, and lateral stiffness.

With respect to inelastic modeling of steel-plate concrete composite shear walls, the existing approaches can be classified as: (1) macroscopic modeling, (2) meso-modeling and (3) microscopic modeling approaches. Macroscopic modeling approaches are developed based on the simplifying assumptions and the observed behavior of structural walls. On the other hand, microscopic modeling approaches use different finite element model formulations and generalized material constitutive relationships. This method can be adapted to simulate a wide range of configurations and behavioral features. Meso-modeling approaches are considered between macroscopic modeling and microscopic modeling approaches. Most of the prior studies focused on the micro finite element modeling of steel-plate concrete composite shear walls using ABAQUS, VecTor2, and LS-DYNA [11,23,24]. The macro model is advantageous because of short-time analysis and less numerical complexities. In this paper, a meso-modeling approach is proposed to predict the response of the steel-plate concrete composite shear walls. A modified fixed strut angle finite element model is developed to simulate the responses of the steel-plate concrete composite shear walls with aspect ratios equal or greater than one. A modified model is utilized to capture the behavior of steel that accounts for tensile fracture, the local buckling of the steel faceplates, and cyclic strength-deterioration. The computational model is then implemented into OpenSees [25]. The analytical model predictions are compared with experimental data.

2. Model Description

The new finite element model is an assembly of a quadrilateral flat shell which is based on the work of Xu and Long, Batoz and Tahar, and Lu et al. [26–28], with a smeared stress–strain formulation applied to describe the behavior of the SCC walls. The constitutive behavior, which relates an average strain field to a smeared stress field, is based on the fixed strut angle model formulation developed by Orakcal et al. [29]. The constitutive behavior is modified to consider tensile fracture, the local buckling of the steel faceplates, and cyclic strength-deterioration.

2.1. Quadrilateral Flat Shell Element Formulation

The planar membrane element GQ12 [26] and the plate bending element [27] are used to construct quadrilateral flat shell element (Fig. 2).

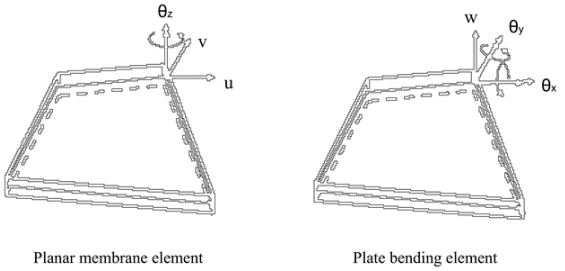

Fig 2. Quadrilateral flat shell element.

Eq.1 defines the nodal displacement vector (q):

$$q=\begin{Bmatrix} q_1 \\ q_2 \\ q_3 \\ q_4 \end{Bmatrix} \quad , \quad q_i = q_i^m + q_i^b \qquad (1)$$

$$q_i^m = \begin{bmatrix} u_i & v_i & \theta_{zi} \end{bmatrix}^T \quad , \quad q_i^b = \begin{bmatrix} w_i & \theta x_i & \theta_{yi} \end{bmatrix}^T$$
$$(i=1,2,3,4) \qquad (2)$$

Where q_i^m is the nodal displacement components of the planar membrane element, q_i^b is the nodal displacement components of the plate bending element, and $\theta_x = \frac{\partial w}{\partial y}, \theta_y = -\frac{\partial w}{\partial x}$. The displacement field of GQ12 is defined as follows:

$$u = u_0 + u_\theta \qquad (3)$$

$$u_0 = N_0 q^m = \sum_{i=1}^{4} \begin{bmatrix} N_i^0 & 0 \\ 0 & N_i^0 \end{bmatrix} \begin{Bmatrix} u_i \\ v_i \end{Bmatrix} ,$$

$$u_\theta = N_\theta q^m = \sum_{i=1}^{4} \begin{bmatrix} N_i^{u\theta} \\ N_i^{v\theta} \end{bmatrix} .\theta_{zi} \qquad (4)$$

Where $N_i^0, N_i^{u\theta}, and\ N_i^{v\theta}$ are the interpolation functions:

$$N_i^0 = \frac{1}{4}\cdot(1+\xi_i\xi)(1+\eta_i\eta) \qquad (5)$$

$$N_i^{u\theta} = \frac{1}{8}\cdot\begin{bmatrix} \xi_i(1-\xi^2)(b_1+b_3\eta_i)(1+\eta_i\eta)+ \\ \eta_i(1-\eta^2)(b_2+b_3\xi_i)(1+\xi_i\xi) \end{bmatrix} \qquad (6)$$

$$N_i^{V\theta} = \frac{-1}{8}\cdot\begin{bmatrix} \xi_i(1-\xi^2)(a_1+a_3\eta_i)(1+\eta_i\eta)+ \\ \eta_i(1-\eta^2)(a_2+a_3\xi_i)(1+\xi_i\xi) \end{bmatrix} \qquad (7)$$

$$a_1 = \frac{1}{4}\sum_{i=1}^{4}\xi_i x_i \qquad a_2 = \frac{1}{4}\sum_{i=1}^{4}\eta_i x_i$$
$$a_3 = \frac{1}{4}\sum_{i=1}^{4}\xi_i\eta_i x_i$$
$$b_1 = \frac{1}{4}\sum_{i=1}^{4}\xi_i y_i \qquad b_2 = \frac{1}{4}\sum_{i=1}^{4}\eta_i y_i$$
$$b_3 = \frac{1}{4}\sum_{i=1}^{4}\xi_i\eta_i y_i \qquad (8)$$

The following relations extract the strain filed contained in a displacement field:

$$\varepsilon_x = \frac{\partial u}{\partial x}\ ,\ \varepsilon_x = \frac{\partial v}{\partial x}\ ,\ \gamma_{xy} = 2\varepsilon_{xy} = \frac{\partial u}{\partial y} + \frac{\partial v}{\partial x} \qquad (9)$$

$$\varepsilon^m = B_m q^m = \sum_{i=1}^{4} B_i^m q_i^m \ ,$$

$$B_i^m = \begin{bmatrix} \frac{\partial N_i^0}{\partial x} & 0 & \frac{\partial N_i^{u\theta}}{\partial x} \\ 0 & \frac{\partial N_i^0}{\partial y} & \frac{\partial N_i^{v\theta}}{\partial y} \\ \frac{\partial N_i^0}{\partial y} & \frac{\partial N_i^0}{\partial x} & \frac{\partial N_i^{u\theta}}{\partial y} + \frac{\partial N_i^{v\theta}}{\partial x} \end{bmatrix} \qquad (10)$$

The element stiffness matrix in the local coordinate system can be obtained by assembling the plate stiffness and the membrane matrices according to the DOFs' sequence:

$$K_b = \iint_A B_B^T D_{bb} B_b \, dA \qquad (11)$$

$$K_m = \int_A B_m^T D_{mm} B_m \, dA \qquad (12)$$

Where D_{bb} and D_{mm} are the material matrix of the plate bending element and the planar membrane element, respectively. See Batoz and Tahar [27] for details about the equations 11 and 12. The large deformation problem is considered using an updated Lagrangian formulation [30].

2.2. The Constitutive Fixed-Strut-Angle Model

An improved version of the fixed-strut-angle-model, developed by Ulugtekin [31] and extended by Orakcal et al. [29], is used in this study to describe the constitutive behavior. A perfect bond between the steel faceplates and the infill concrete was assumed for developing the numerical model. The implemented uniaxial constitutive stress-strain relationship for steel is modified to consider tensile fracture, the local buckling of the steel faceplates, and cyclic strength-deterioration. The Fixed-Strut-Angle model does not consider the effect of slip deformations. The constitutive behavior model has three stages: (a) un-cracked concrete, (b) formation of the first crack, and (c) formation of the second crack. In the un-cracked state of concrete, its stress-strain behavior in the fixed-strut-angle-model is calculated using a rotating-principal stress-direction approach [32,33]. After transforming the strain field into principal strain directions, uniaxial stress–strain relationships are utilized to obtain principal stresses in concrete. Two coefficients are calculated and applied to incorporate compression softening and biaxial damage effect [34–36]:

$$\beta_{damage} = (1 - 0.4 \cdot \frac{\varepsilon_{\perp \max}}{\varepsilon_c}) \qquad (13)$$

$$\beta_m = \frac{1}{1 + k_c}\ ,\ K_c = 0.27 \cdot (\frac{\varepsilon_1}{\varepsilon_0} - 0.37) \geq 1.0 \qquad (14)$$

Where $\varepsilon_{\perp \max}$, ε_c, ε_0, and ε_1 are the maximum value of the compressive strain, the peak compressive strain, the strain corresponding to peak stress of concrete in compression, and the tensile strain in the principal tensile stress direction, respectively. When the principal tensile strain in concrete first exceeds the monotonic cracking strain of concrete, the first crack develops, and this principal direction ($\theta_{cr,A}$) remains unchanged for all of the following loading stages as the first "fixed strut" until the second crack forms. A uniaxial stress-strain relationship for concrete can be utilized in parallel and perpendicular to the first strut (principal stress directions).

It is assumed that the second "fixed strut" (second crack) will form perpendicular to the direction of the first crack. For further loading stages, these two independent struts of the concrete will work as interchanging tension/compression struts. For all loading stages, biaxial softening effects (β_m, β_{damage}) are considered. An aggregate interlocking action stems from sliding along the cracks. Therefore, a friction-based relationship is used for modeling shear aggregate interlock. When the concrete normal stress perpendicular to the crack is compressive, the shear stress, which is caused by the shear aggregate interlock, is calculated by the product of the concrete normal stress perpendicular to the crack and a friction coefficient. When the crack is open (the normal stress perpendicular to the crack is tensile), the shear stress is set to zero. The linear unloading/reloading slope is $0.4E_c$ (E_c is the concrete elastic modulus) (Fig. 3). To consider the dowel effect of the steel

faceplate, a linear-elastic constitutive model (Kolozvari et al. [37–39]) is incorporated.

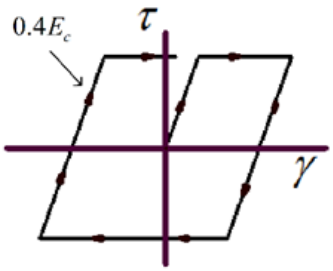

Fig 3. Shear Aggregate Interlock model [40,41].

2.2.1. Constitutive Model For Concrete

A refined relationship proposed by Chang and Mander [42] is used for concrete. The uniaxial constitutive model captures gradual crack closure, the progressive degradation of stiffness, concrete crushing, tension stiffening, and hysteretic behavior. Schematic drawing of the hysteretic uniaxial constitutive model is shown in Fig 4. More details about this hysteretic uniaxial constitutive model can be found in [37,39].

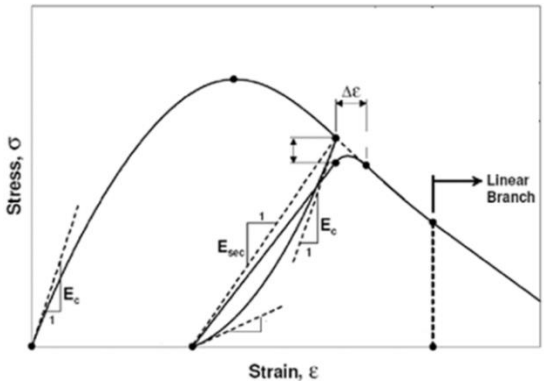

Fig 4. Schematic drawing of the constitutive model for concrete [37,39].

Considering the size influence on the strain of concrete components results in a precise and reliable estimation of the concrete model's softening branch [43,44]. Based on the localization phenomenon, Markeset and Hillerborg [45] suggested an empirical model to adjust the ultimate strain (ε_{cu}):

$$\varepsilon_{cu,l} = \varepsilon_{cu} + \frac{w}{L_c} \quad (15)$$

Where L_c is the length of the component and w is a calibration value in [0.4, 0.7].

2.2.2. Constitutive Model For Steel

The failure mechanism of the SCC shear wall is characterized, among other things, by concrete crushing at the wall base, local buckling at the corners of the steel faceplates, and local buckling between shear stud locations. Since the constitutive model for steel does not capture any form of strength degradation, the original formulation is modified by implementing a new constitutive model used for steel material based on the work of Bosco et al. and Kunnath et al. [46–48] (Figure 5).

The general hysteretic stress-strain relationship is as follows:

$$\sigma^* = b\varepsilon^* + \frac{(1-b)\varepsilon^*}{(1+\varepsilon^{*R})^{1/R}} \;,\; \varepsilon^* = \frac{\varepsilon - \varepsilon_r}{\varepsilon_0 - \varepsilon_r} \;,$$
$$\sigma^* = \frac{\sigma - \sigma_r}{\sigma_0 - \sigma_r} \;,\; R = R_0 - \frac{a_1\varepsilon^*}{a_2 + \varepsilon^*} \quad (16)$$

Where σ_r, R, ε_r, and b are the stress at the point of strain reversal, the curvature parameter, the strain at the point of strain reversal, and the strain hardening ratio, respectively. R_0, a_1 and a_2 are experimentally determined parameters. Values of $R_0 = 20, a_1 = 18.5, a_2 = 0.15$ and $R_0 = 20, a_1 = 18.5, a_2 = 0.0015$ were recommended by Menegotto and Pinto [40] and Elmorsi et al. [49], respectively. The formulation of Pugh [50] is adopted using the OpenSees MinMax wrapper to simulate full buckling. To model low-cycle fatigue

and strength degradation, the so-called Coffin-Manson type expressions [47] are implemented in the formulation of steel material:

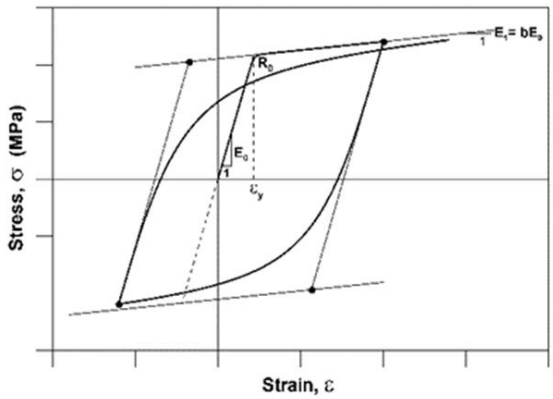

Fig 5. Hysteretic model of the steel material [37,39].

$$\varepsilon^p = C_f (2N_f)^{-\alpha},\ \varepsilon^p = C_d (f_{SR})^{\beta} \qquad (17)$$

Where ε^p, C_f, $2N_f$, α, C_d, f_{SR}, and β are plastic strain amplitude, material constants, number of half-cycles to failure, material constants, strength loss factor per cycle , and material constants. The values of the material constants are taken as $\alpha = 0.44$, $C_f = 0.12$, $\beta = 0.45$, and $C_d = 0.2$ following Kunnath et al. [47]. The buckling strength and strain are estimated using the equations (Eqs.18 and19) proposed by Bai et al. [51] and Akiyama et al. [52].

$$\sigma_b = \frac{\pi^2 E_s}{12k^2 (\frac{B}{t_s})^2} \le \sigma_y \qquad (18)$$

$$\frac{\varepsilon_b}{\varepsilon_y} = 6.2a^{-1.4} + 1 \ ,\ a = (\frac{1}{1.32} \cdot \frac{B}{t_s})^2 \varepsilon_y \qquad (19)$$

Where σ_b, B, E_s, t_s, k, σ_y, ε_b, and ε_y are the buckling strength, the stud spacing, the elastic modulus of the steel faceplate, the thickness of the steel faceplate, the effective length ratio, the yield stress of steel plate, the steel strain at buckling, and the steel strain at yielding, respectively. These equations are validated by Haghi et al. [53] for steel plate.

2.3. Mesh Sensitivity

Descending parameters and fracture energies of the materials and mesh grid size may affect the computed response of each wall. To determine the appropriate descending parameters for the localized compressive zone, the model proposed by Coleman and Spacone [54] was utilized. The values recommended by Jansen and Shah [55] are used for the compressive fracture energy of concrete. More details on the mesh sensitivity procedure can be found in [54] and [55]. As an example, the DSCW-2 specimen was discretized. Two different meshes were considered. Model 1 had 7 elements in the horizontal direction and 5 elements in the vertical direction. Model 2 had 12 elements in the horizontal direction and 10 elements in the vertical direction. Figure 6 shows the effect of mesh configuration for Model 1 and Model 2 on experimental data. Figure 6 illustrates the fact that utilizing a finer mesh (Model 2) did not offer better performance.

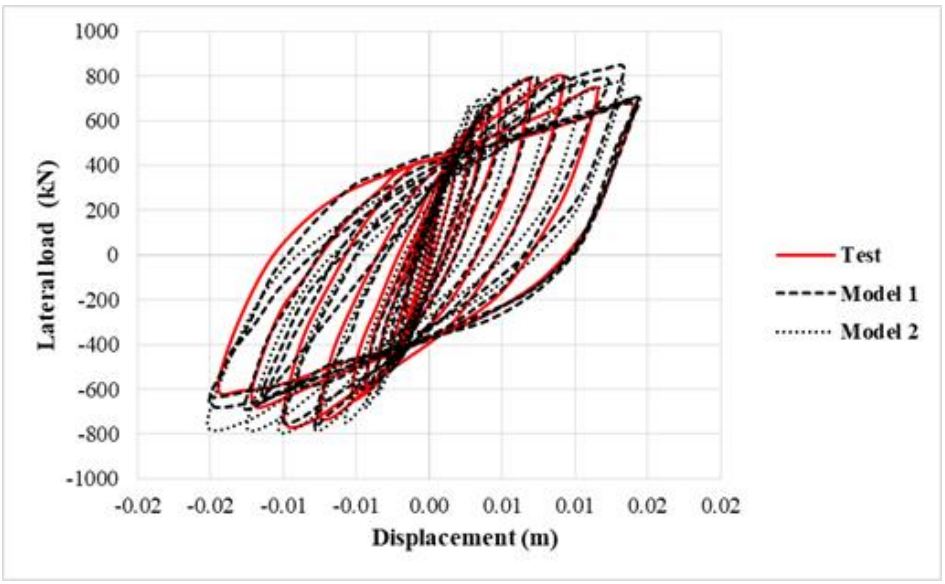

b

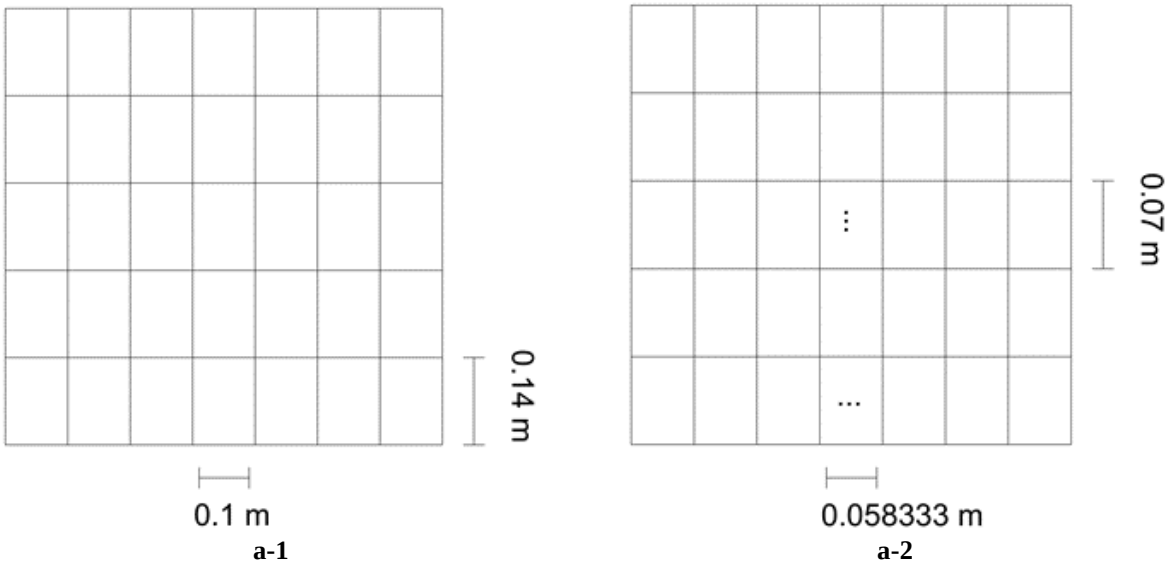

a-1 a-2

Fig 6. DSCW-2 specimen: a) finite element mesh configuration, b) Load-displacement response.

3. Numerical Validations

This section presents several experiments of the SCC walls which are used to validate the proposed numerical model. The steel plate-concrete composite walls subjected to quasi-static cyclic lateral loading are used. The dataset included fifteen steel plate-concrete composite wall specimens from five experimental test programs conducted by researchers around the world. Tables 1-3 present the properties of the test specimens. The tensile strength and tension strain of the concrete, for all specimens, are considered equal to $0.31\sqrt{f_c^{'}[MPa]}$ [56] and 0.0001, respectively, where $f_c^{'}$ is uniaxial compressive stress of unconfined concrete.

Important points which should be mentioned are as follows:

1. The peak compressive stress of confined concrete was calibrated according to the confinement model by Mander et al. [57].
2. SCC walls which have the side and insert plates in the boundary elements, the plates are modeled using truss elements and the proposed constitutive model for steel material.
3. Both the infill steel panel and boundary frame members are modeled using the four-node, general purpose shell element.
4. A perfect bond between the steel faceplates and the infill concrete is assumed.
5. In this study, the specimens (from five experimental test programs) which have the same configuration and material are ignored.

Table 1. Properties of the steel plate-concrete composite wall specimens.

No.	Researcher	Specimens ID	Cross section (mm × mm)	Aspect ratio	Axial load ratio	Steel plate thickness (mm)	
						Boundary	web
1	Cho [58]	SXC1	400 X 150	2.4	0	-	3
2	Ma [59]	DSCW-2	700 X 100	1.0	0.1	3	3
3	Epackachi [8,60,61]	SC1	1524 X 305	1.0	0	-	4.8
4		SC2	1524 X 305	1.0	0	-	4.8
5		SC4	1524 X 229	1.0	0	-	4.8
6	Cheng & Zhou [62]	CCSP-1	620 X 86	1.5	0.4	6	3
7		CCSP-3	620 X 86	1.5	0.3	6	3
8		CCSP-7	620 X 106	2.5	0.3	6	3
9		CCSP-9	620 X 86	1.5	0.3	C40X40X40&6	3
10	Nie [63]	CFSCW-1	1284 X 214	2.0	0.37	5	5
11		CFSCW-2	1284 X 214	2.0	0.37	5	5
12		CFSCW-4	1284 X 214	2.0	0.36	4	4
13		CFSCW-5	1284 X 214	2.0	0.37	3	3
14		CFSCW-8	1284 X 214	2.0	0.32	6	4
15		CFSCW-11	750 X 125	1.5	0.33	3	3

Table 2. Properties of the steel material of the wall specimens.

No.	Researcher	Specimens ID	Web		Boundary	
			$\sigma_b(MPa)$	$\varepsilon_b(mm/mm)$	$\sigma_b(MPa)$	$\varepsilon_b(mm/mm)$
1	Cho [58]	SXC1	400	0.01	-	-
2	Ma [59]	DSCW-2	334	0.011	310	0.011
3	Epackachi [8,60,61]	SC1	248	0.038	-	-
4		SC2	248	0.0013	-	-
5		SC4	248	0.028	-	-
6	Cheng & Zhou [62]	CCSP-1	322	0.069	322	0.199
7		CCSP-3	322	0.011	322	0.199
8		CCSP-7	322	0.011	322	0.097
9		CCSP-9	322	0.011	322	0.199
10	Nie [63]	CFSCW-1	306	0.241	306	0.241
11		CFSCW-2	306	0.241	306	0.241
12		CFSCW-4	351	0.118	351	0.118
13		CFSCW-5	443	0.05	443	0.05
14		CFSCW-8	351	0.118	363	0.118
15		CFSCW-11	443	0.218	443	0.218

Table 3. Properties of the concrete material of the wall specimens.

No.	Researcher	Specimens ID	Uniaxial compressive stress of concrete	
			Unconfined (MPa)	Confined (MPa)
1	Cho [58]	SXC1	35	-
2	Ma [59]	DSCW-2	53	62
3	Epackachi [8,60,61]	SC1	30.3	-
4		SC2	30.3	-
5		SC4	36.6	-
6	Cheng & Zhou [62]	CCSP-1	24	34
7		CCSP-3	24	31
8		CCSP-7	24	31
9		CCSP-9	24	34
10	Nie [63]	CFSCW-1	73.1	103
11		CFSCW-2	71.7	101
12		CFSCW-4	75.4	103.8
13		CFSCW-5	73.7	99.4
14		CFSCW-8	74	102
15		CFSCW-11	66.3	95.1

A brief discussion of the results for each of the fifteen experimental specimens, which are grouped by experimental program, are provided below:

3.1. SXC1 Specimen (Cho's SCC Wall)

The SXC1 specimen tested by Cho et al. [58] had no boundary elements and showed base-plate flexibility. Therefore, five support springs are utilized to model the initial stiffness of the SXC1 specimen. Each spring has an axial stiffness of $79 kN/mm$. Additionally, horizontal flexural cracks as well as shear cracks and the buckling of steel plates were reported by Cho et al. [58]. Figure 7 shows the numerical results and the experimental results. Comparison of experimental data and analytical results of the SXC1 specimen shows that the proposed numerical model slightly underestimates pinching characteristics of the response. The numerical model predicts the maximum strength, with an average error of 11%. From Figure 7 shows the proposed model simulates well the lateral stiffness of the specimen for all the applied drift levels. The numerical model captures initial stiffness successfully using the five support springs for considering the base-plate flexibility. The effect of the buckling of the steel faceplates near the base of the wall on the lateral load capacity is captured.

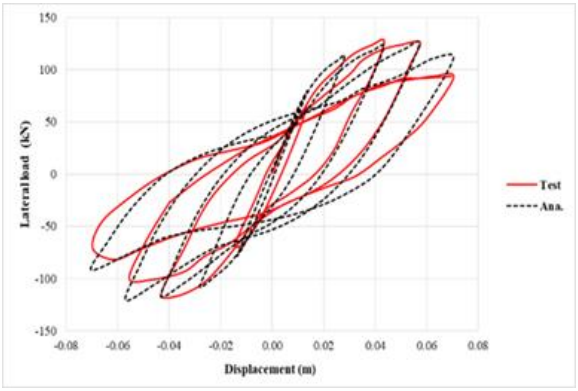

Fig 7. Load-displacement response of SXC1 specimen.

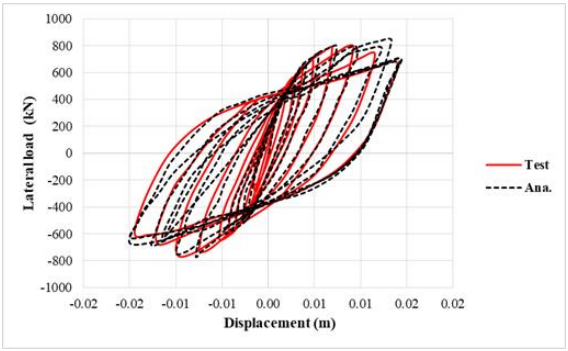

Fig 8. Load-displacement response for DSCW-2 specimen.

3.2. DSCW-2 Specimen (Ma's SCC Wall)

Ma et al. [59] tested three steel plate-concrete composite walls without boundary elements. The walls were in 1-4 scale. In this study, the specimens which have the same configuration and material are ignored. The failure modes of the DSCW-2 specimen with a low shear-to-span ratio under the combined action of the cycle's horizontal and axial compression load consist of local buckling of steel plates and compressive crushing of concrete. The experimentally-measured and computed numerical load-displacement responses of the specimen are plotted in Figure 8. It can be found from the figure that the result of the proposed model matches the experimental result very well and the characteristics of the hysteretic loops, including cyclic stiffness degradation and the energy dissipation, are predicted. The numerical model overestimates the experimentally-measured lateral load at 1.6% drift ratio in the positive loading direction.

3.3. Epackachi's SCC Wall

Epackachi et al. [60,61] presented the results for a series of tests using SCC walls. Damages to SCC walls were concrete crushing, buckling of the steel faceplates, and tearing of the steel faceplates. To model the connection between a steel plate-concrete composite wall and its foundation, six support springs are utilized. The stiffness of each spring for SC1, SC2, and SC4, is $7.28\times10^{8}\frac{N}{m}$, $3.28\times10^{8}\frac{N}{m}$, $3.28\times10^{8}\frac{N}{m}$, respectively. The comparison of the lateral load versus top displacement responses by simulation and experiment of the three specimens is presented in Figure 9. Specimen SC4 exhibits greater strength and deformation capacity (with an average error of 17%) in the simulation than is observed experimentally at the loading cycle preceding the ultimate loading cycle in the positive loading direction. Important features of the top displacement-lateral load diagrams such as the unloading and reloading force path and cyclic stiffness degradation are well predicted for other specimens. The hysteretic curves also demonstrate a slight pinching effect. The numerical model tends to slightly underestimate pinching.

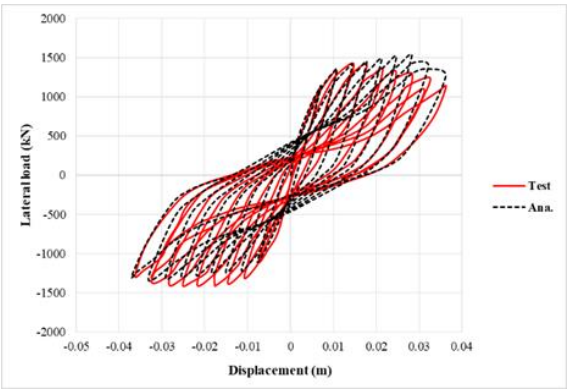

b-1) SC1 specimen

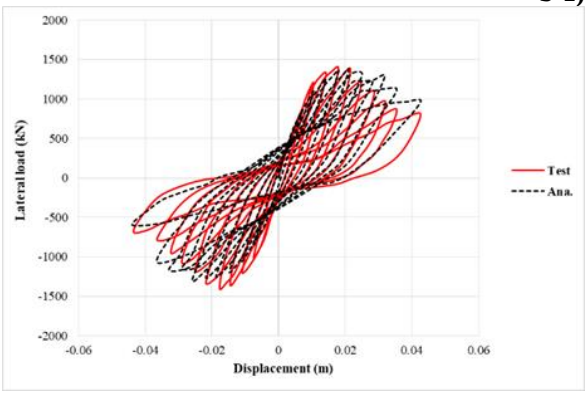

b-2) SC2 specimen

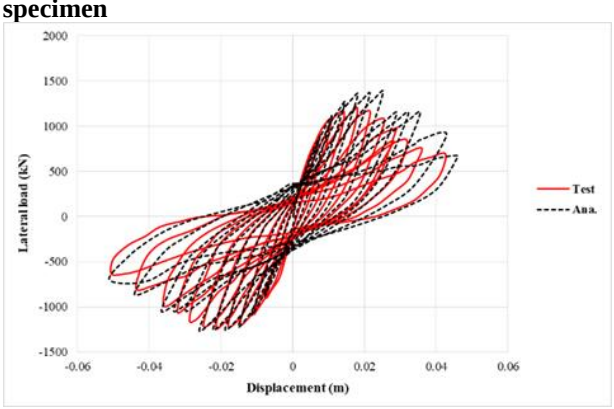

b-3) SC4 specimen

Fig 9. Load-displacement response for Epackachi's SC walls.

Turning now to the experimental evidence on the vertical strain distribution in the steel faceplate, the analytically-predicted and experimentally-measured vertical strain distribution of the SC4 steel faceplate for the drift levels of 0.5% and 0.95% are presented in Figure 10. At 0.5% and 0.95% drift levels, both tensile and compressive strains at the steel faceplate are predicted with reasonable accuracy (with a mean error of 14%). Figure 11 shows the analytically-predicted and experimentally-measured hysteretic damping ratio at different drift levels for SC4 specimen. The results obtained from the experimental and numerical data have an average error of 8.4 %.

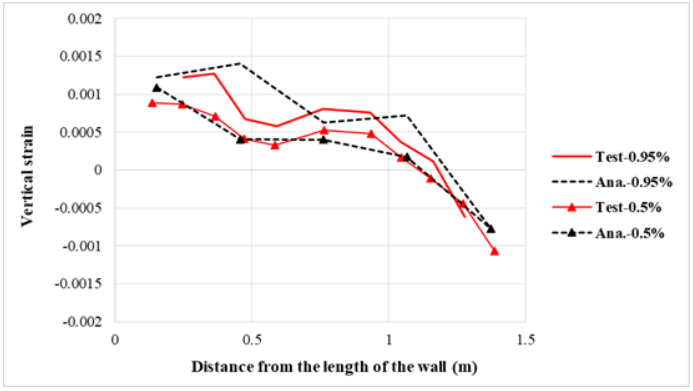

Fig 10. Vertical strain distribution in the steel faceplate.

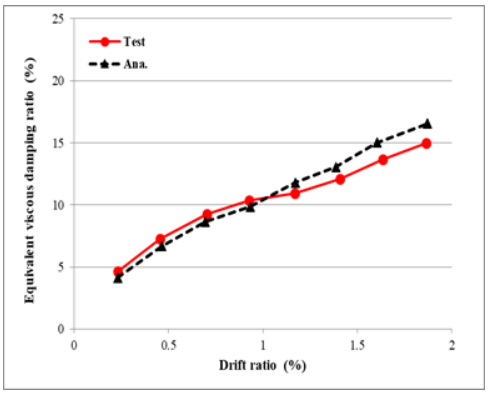

Fig 11. Equivalent viscous damping ratio for SC4 specimen.

3.4. Cheng and Zhou's SCC Wall

Cheng and Zhou [62] conducted an extensive study of experimental SCC wall specimens. The cyclic loading tests were conducted on ten SCC wall specimens with aspect ratios of 1.5 - 2.5. The SCC walls had boundary channel columns. In this study, the specimens which have the same section and material are ignored. Figure 12 shows the analytical results and the laboratory test results for each wall. For CCSP-3 of CCSP-7 specimens, simulated stiffness is greater than the measured stiffness. The disparity is likely due to the flexibility of the connection between a steel plate-concrete composite wall and its foundation as well as excessive shrinkage. Barkhordari et al. [64] stated that pretest micro-cracking close to the base of the walls as a result of the restrained shrinkage and early-stage cracking at the wall foundation can lead to a wrong assessment of stiffness. Currently, OpenSees has presented no valid option to take into account the shrinkage [25]. Epackachi [60] showed that disregarding not-so-rigid base-wall connections in the nonlinear analysis of the SCC walls leads to inappropriate initial stiffness calculation. Also, many reasons, such as imperfections of specimens and customizable initial stiffness in the material model used, can result in this difference. It can be found from the Figure 12 that cyclic characteristics of the response, including initiation of strength degradation, plastic displacements, and stiffness degradation behavior can be reproduced by the proposed numerical model.

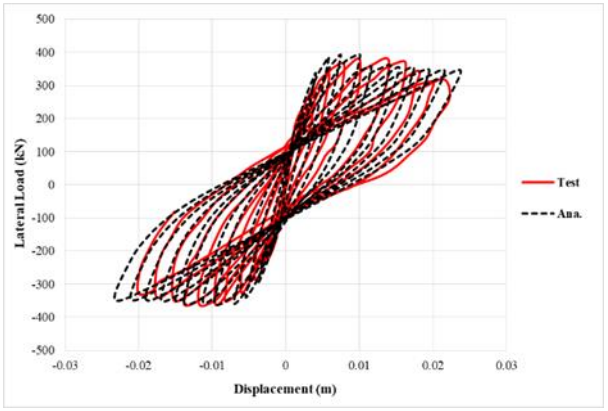

b-1) CCSP-1

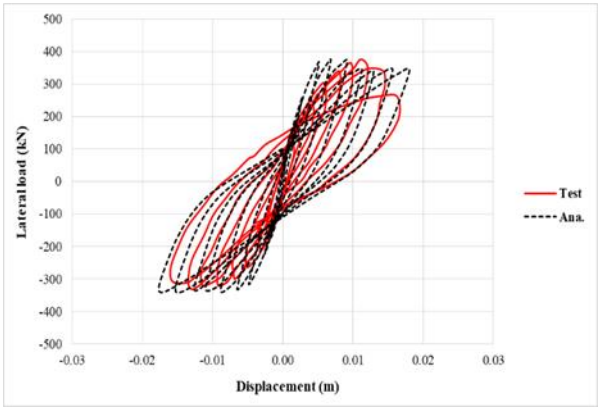

b-2) CCSP-3

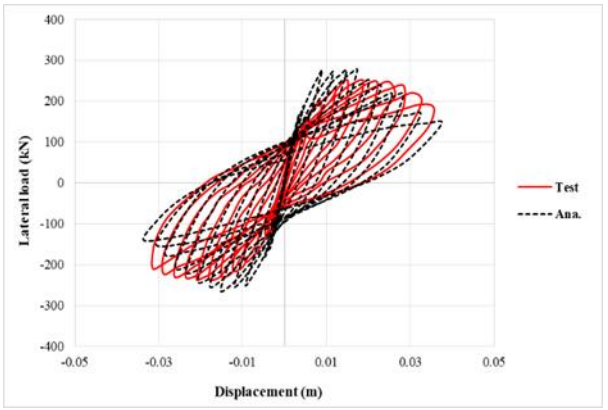

b-2) CCSP-7

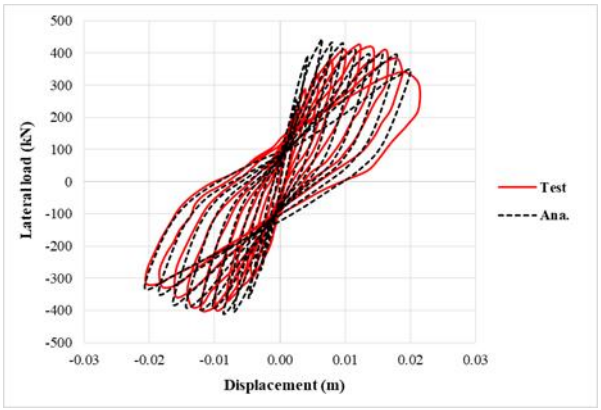

b-2) CCSP-9

Fig 12. Load-displacement response for Cheng and Zhou's SCC walls.

3.5. Nie's SCC Wall

Nie et al. [63] performed quasi-static cyclic testing on twelve composite wall specimens to evaluate the overall in-plane performance of the wall. Six out of twelve specimens tested by Nie et al. [63] are selected in this paper. The specimens with the same material properties and sections are not considered in this paper. Specimens CFSCW-1, CFSCW-2, CFSCW-4, CFSCW-5, CFSCW-8, and CFSCW-11 failed in a progression of fracture initiation, fracture propagation, and local buckling. Local buckling occurred earlier for CFSCW-4 and CFSCW-5 since thinner plates were used for these specimens. During the test, for specimens CFSCW-5 and CFSCW-8, the steel plates fractured at the locations that approximate 170 mm from the wall base. The experimentally-measured and the computed numerical responses of the Nie's SCC walls are shown in Figure 13. The results of the numerical model are in good agreement with those obtained in the experiments in terms of the pinching of the hysteresis loops and stiffness degradation. Only for CFSCW-4, the model underestimates the pinching of the hysteresis loops. The wall lateral load capacity is overestimated by the proposed model during the last cycle for CFSCW-2, CFSCW-4, and CFSCW-5 specimens with a mean error of 13.1%. Table 4 compares the (peak) lateral load capacity of the analytical models and the experimental results. The predictions are obtained with acceptable accuracy using proposed model for the experimentally measured lateral load.

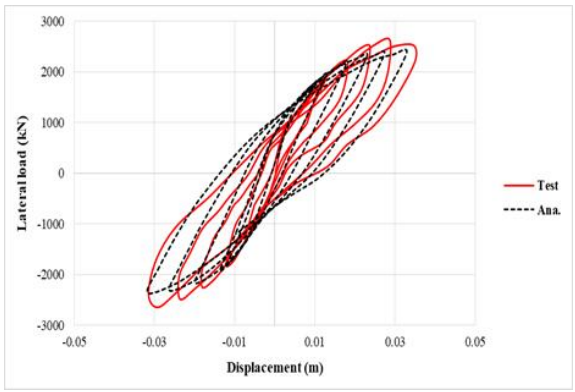

b-1) CFSCW-1

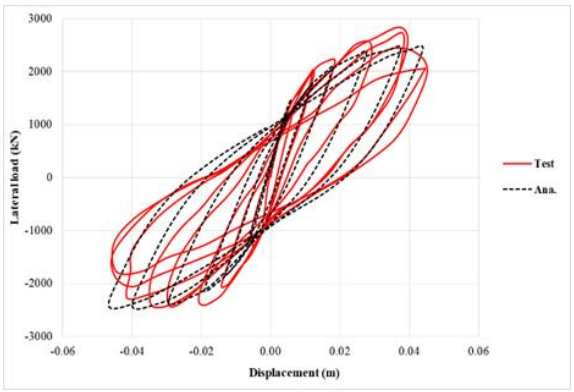

b-2) CFSCW-2

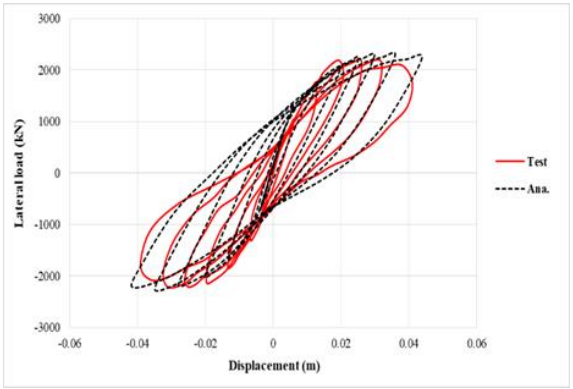

b-3) CFSCW-4

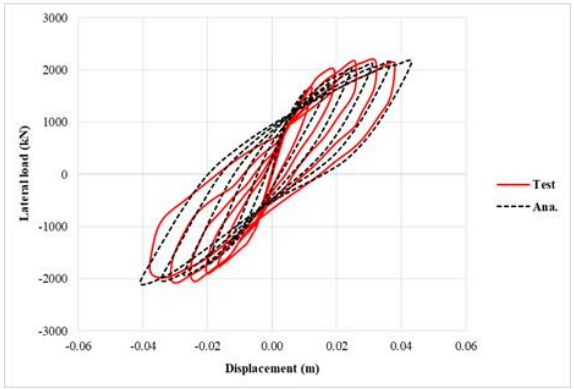

b-4) CFSCW-5

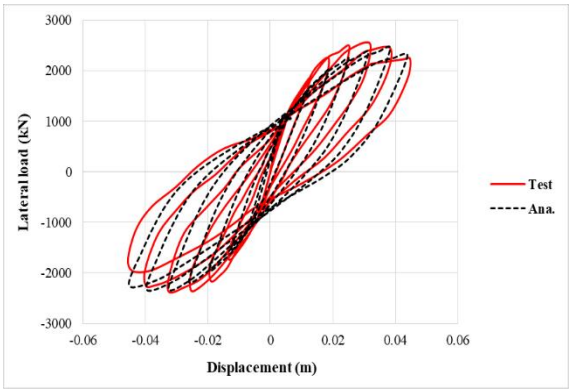

b-5) CFSCW-8

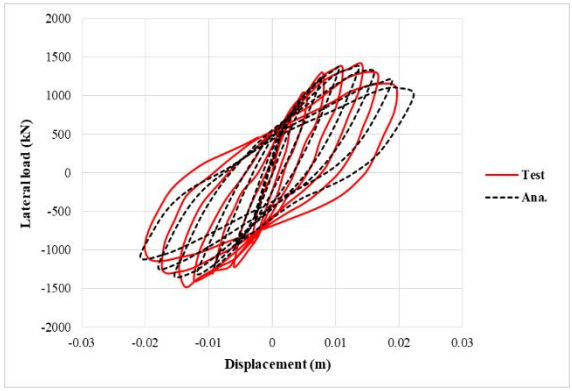

b-6) CFSCW-11

Fig 13. Load-displacement response for Nie's SCC walls.

Table 4. Comparing the maximum capacity obtained with the numerical model and experiment.

		Positive Direction (kN)			Negative Direction (kN)		
		Test	Num.	Num./test	Test	Num.	Num./test
1	SXC1	126	124	0.98	105	117	1.11
2	DSCW-2	794	767	0.97	770	740	0.96
3	SC1	1410	1500	1.06	1400	1305	0.93
4	SC2	1396	1354	0.97	1408	1260	0.89
5	SC4	1210	1350	1.12	1215	1265	1.04
6	CCSP-1	380	390	1.03	365	354	0.97
7	CCSP-3	375	345	0.92	320	338	1.06
8	CCSP-7	240	270	1.13	235	260	1.11
9	CCSP-9	416	395	0.95	397	410	1.03
10	CFSCW-1	2630	2365	0.90	2640	2360	0.89
11	CFSCW-2	2830	2435	0.86	2270	2444	1.08
12	CFSCW-4	2200	2220	1.01	2090	2200	1.05
13	CFSCW-5	2100	2127	1.01	1905	2090	1.10
14	CFSCW-8	2542	2360	0.93	2250	2330	1.04
15	CFSCW-11	1415	1365	0.96	1480	1345	0.91

3.6. The Effect of Stress–Strain Models For Steel Material

In this section, the analytical model of the CCSP-9 specimen is analyzed again using the conventional model for steel material (OpenSees-Steel02 Material, Filippou et al. [48]). Figure 14 shows the response of the proposed model with two different constitutive stress-strain relationship for steel material. A comparison of Figure 14-a and 14-b shows that the numerical model without considering buckling, low-cycle fatigue degradation, and tensile fracture, overestimates lateral load capacity and pinching behavior.

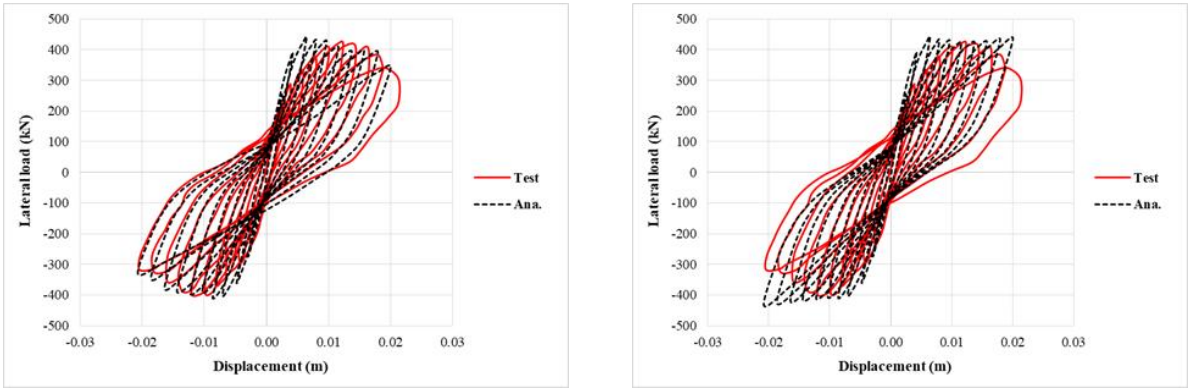

Fig 14. Load-deformation response of the CCSP-9 a) with, and b) without considering buckling, low-cycle fatigue degradation, and tensile fracture.

3.7. Sensitivity Analysis

A method that is used here for the calculation of the global sensitivity indices is based on the work of Vu-Bac et al. [65]. The method is variance-based sensitivity indices for models with dependent variables [66]. Figure 15 plots the total sensitivity indices and the parameters that characterize the parameter space of interest. The slenderness ratio is characterized as the ratio of max distance between two neighboring connectors to the thickness of the steel faceplate. Figure 15 indicates that the aspect ratio, axial load, and steel-plate thickness are the dominant parameters that contribute to the lateral strength of the SCC wall.

4. Limitations

Although the suggested modeling methodology appears to correctly estimate the nonlinear cyclic response of composite shear walls, its limitations must be examined: (1) the proposed modeling technique is designed to estimate the hysteretic response of SCC walls. Finite element models will be required for comprehensive local responses such as damage states, (2) the current modeling technique is restricted to cases where the assumptions (a perfect bond between the steel faceplates and the infill concrete) in the proposed numerical model formulations are valid.

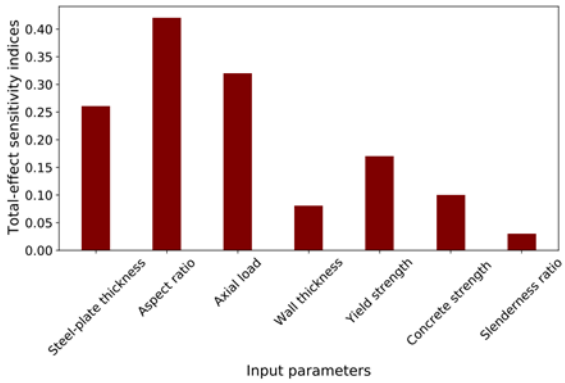

Fig 15. Sensitivity analysis.

5. Conclusion

This paper presents information about the formulation and validation of a new semi-macro modified fixed strut angle finite element model for seismic analysis of the double skin composite walls. A quadrilateral flat shell element, which can model the effect of large deformation, and an effective constitutive model-referred to as the “fixed strut angle model” were used in this paper. The constitutive models captured tensile fracture, local/global buckling, low-cycle fatigue degradation of the steel plate, compression-softening, and tension-stiffening. To validate the developed

numerical model, fifteen steel plate-concrete composite walls were used as case studies. Comparisons between experimentally-measured lateral load-displacement responses of the walls and the predicted responses by the numerical model revealed that the proposed model was capable of appropriately modeling the cyclic load-displacement response attributes of wall specimens.

References

[1] Sarir P, Chen J, Asteris PG, Armaghani DJ, Tahir MM. Developing GEP tree-based, neuro-swarm, and whale optimization models for evaluation of bearing capacity of concrete-filled steel tube columns. Eng Comput 2021;37:1–19. https://doi.org/10.1007/s00366-019-00808-y.

[2] Barkhordari MS, Massone LM. Failure Mode Detection of Reinforced Concrete Shear Walls Using Ensemble Deep Neural Networks. Int J Concr Struct Mater 2022;16:33. https://doi.org/https://doi.org/10.1186/s40069-022-00522-y.

[3] López CN, Massone LM, Kolozvari K. Validation of an efficient shear-flexure interaction model for planar reinforced concrete walls. Eng Struct 2022;252:113590. https://doi.org/10.1016/j.engstruct.2021.113590.

[4] Kolozvari K, Arteta C, Fischinger M, Gavridou S, Hube M, Isakovic T, et al. Comparative study of state-of-the-art macroscopic models for planar reinforced concrete walls 2018. https://doi.org/https://doi.org/10.14359/51710835.

[5] Naderpour H, Sharei M, Fakharian P, Heravi MA. Shear Strength Prediction of Reinforced Concrete Shear Wall Using ANN, GMDH-NN and GEP. J Soft Comput Civ Eng 2022;6:66–87. https://doi.org/10.22115/scce.2022.283486.1308.

[6] Barkhordari MS, Massone LM. Efficiency of deep neural networks for reinforced concrete shear walls failure mode detection. 2022 27th Int. Comput. Conf. Comput. Soc. Iran, 2022, p. 1–4. https://doi.org/10.1109/csicc55295.2022.9780477.

[7] Yang Y, Cho IH. Multiple Target Machine Learning Prediction of Capacity Curves of Reinforced Concrete Shear Walls. J Soft Comput Civ Eng 2021;5:90–113. https://doi.org/10.22115/scce.2021.314998.1381.

[8] Epackachi S, Whittaker AS, Varma AH, Kurt EG. Finite element modeling of steel-plate concrete composite wall piers. Eng Struct 2015;100:369–84. https://doi.org/10.1016/j.engstruct.2015.06.023.

[9] Ozaki M, Akita S, Osuga H, Nakayama T, Adachi N. Study on steel plate reinforced concrete panels subjected to cyclic in-plane shear. Nucl. Eng. Des., vol. 228, 2004, p. 225–44. https://doi.org/10.1016/j.nucengdes.2003.06.010.

[10] Vecchio FJ, McQuade I. Towards improved modeling of steel-concrete composite wall elements. Nucl Eng Des 2011;241:2629–42. https://doi.org/10.1016/j.nucengdes.2011.04.006.

[11] Wong PS, Vecchio FJ, Trommels H. Vector2 & Formworks user's manual second edition. Univ Toronto, Canada 2013.

[12] Emrani SM, Epackachi S, Tehrani P, Imanpour A. A fibre-based modelling technique for the seismic analysis of steel–concrete composite shear walls. Can J Civ Eng 2022;49:993–1007. https://doi.org/10.1139/cjce-2021-0125.

[13] Xiaowei M, Jianguo N, Muxuan T. Nonlinear finite-element analysis of double-skin steel-concrete composite shear wall structures. Int J Eng Technol 2013;5:648.

[14] Rafiei S, Hossain KMA, Lachemi M, Behdinan K, Anwar MS. Finite element modeling of double skin profiled composite shear wall system under in-plane loadings. Eng Struct 2013;56:46–57. https://doi.org/10.1016/j.engstruct.2013.04.014.

[15] Ali A, Kim D, Cho SG. Modeling of nonlinear cyclic load behavior of I-shaped composite steel-concrete shear walls of nuclear power plants. Nucl Eng Technol 2013;45:89–98. https://doi.org/10.5516/NET.09.2011.055.

[16] Varma AH, Zhang K, Chi H, Booth P, Baker T. In-plane shear behavior of SC composite walls: theory vs. experiment. Proc. 21st IASMiRT Conf. (SMiRT 21), 2011.

[17] Varma AH, Malushte SR, Sener KC, Lai Z. Steel-plate composite (SC) walls for safety related nuclear facilities: Design for in-plane forces and out-of-plane moments. Nucl Eng Des 2014;269:240–9. https://doi.org/10.1016/j.nucengdes.2013.09.019.

[18] Kurt E, Whittaker A, Varma A, Booth P. SC wall piers and basemat connections: numerical investigation of behavior and design 2013.

[19] Nie JG, Ma XW, Tao MX, Fan JS. Nonlinear finite-element analysis of double-skin steel-concrete composite shear wall structures. Harbin Gongye Daxue Xuebao/Journal Harbin Inst Technol 2012;44:147–51. https://doi.org/10.7763/ijet.2013.v5.634.

[20] Construction AI of S. Specification for safety-related steel structures for nuclear facilities, supplement No. 1 2014.

[21] Nguyen NH, Whittaker AS. Numerical modelling of steel-plate concrete composite shear walls. Eng Struct 2017;150:1–11. https://doi.org/10.1016/j.engstruct.2017.06.030.

[22] Wang W, Ren Y, Han B, Ren T, Liu G, Liang Y. Seismic performance of corrugated steel plate concrete composite shear walls. Struct Des Tall Spec Build 2019;28:e1564. https://doi.org/10.1002/tal.1564.

[23] Hallquist JO. LS-DYNA keyword user's manual. Livermore Softw Technol Corp 2007;970:299–800.

[24] Wright W. User's manual for LEWICE version 3.2. NASA CR-214255 2008.

[25] McKenna F, Scott MH, Fenves GL. Nonlinear Finite-Element Analysis Software Architecture Using Object Composition. J Comput Civ Eng 2010;24:95–107. https://doi.org/10.1061/(asce)cp.1943-5487.0000002.

[26] Yuqiu XYL. quadrilateral membrane element with vertex rotational freedom from generalized compatible condition [j]. Eng Mech 1993;3.

[27] Batoz J, Tahar M Ben. Evaluation of a new quadrilateral thin plate bending element. Int J Numer Methods Eng 1982;18:1655–77.

[28] Lu X, Tian Y, Cen S, Guan H, Xie L, Wang L. A High-Performance Quadrilateral Flat Shell Element for Seismic Collapse Simulation of Tall Buildings and Its Implementation in OpenSees. J Earthq Eng 2018;22:1662–82. https://doi.org/10.1080/13632469.2017.1297269.

[29] Orakcal K, Massone LM, Ulugtekin D. A Hysteretic Constitutive Model for Reinforced Concrete Panel Elements. Int J Concr Struct Mater 2019;13:51.

https://doi.org/10.1186/s40069-019-0365-9.

[30] Belytschko T, Liu WK, Moran B, Elkhodary K. Nonlinear finite elements for continua and structures. John wiley & sons; 2013.

[31] Uluğtekin D. Analytical modeling of reinforced concrete panel elements under reversed cyclic loadings. Boğaziçi University, 2010.

[32] Vecchio FJ, Collins MP. The modified compression-field theory for reinforced concrete elements subjected to shear. ACI J 1986;83:219–31.

[33] Pang X-BD, Hsu TTC. Behavior of reinforced concrete membrane elements in shear. Struct J 1995;92:665–79.

[34] Mansour M, Hsu TTC. Behavior of Reinforced Concrete Elements under Cyclic Shear. II: Theoretical Model. J Struct Eng 2005;131:54–65. https://doi.org/10.1061/(asce)0733-9445(2005)131:1(54).

[35] Mansour M, Hsu TTC. Behavior of Reinforced Concrete Elements under Cyclic Shear. I: Experiments. J Struct Eng 2005;131:44–53. https://doi.org/10.1061/(asce)0733-9445(2005)131:1(44).

[36] Vecchio FJ, Collins MP. Compression response of cracked reinforced concrete. J Struct Eng 1993;119:3590–610.

[37] Kolozvari K, Tran TA, Orakcal K, Wallace JW. Modeling of Cyclic Shear-Flexure Interaction in Reinforced Concrete Structural Walls. II: Experimental Validation. J Struct Eng 2015;141:04014136. https://doi.org/10.1061/(asce)st.1943-541x.0001083.

[38] Kolozvari K, Orakcal K, Wallace JW. Shear-flexure interaction modeling for reinforced concrete structural walls and columns under reversed cyclic loading. Pacific Earthq Eng Res Center, PEER Rep 2015.

[39] Kolozvari K, Orakcal K, Wallace JW. Modeling of Cyclic Shear-Flexure Interaction in Reinforced Concrete Structural Walls. I: Theory. J Struct Eng 2015;141:04014135. https://doi.org/10.1061/(asce)st.1943-541x.0001059.

[40] Kolozvari K. Analytical modeling of cyclic shear-flexure interaction in reinforced concrete structural walls. UCLA, 2013.

[41] Kolozvari K, Orakcal K, Wallace JW. New opensees models for simulating nonlinear flexural and coupled shear-flexural behavior of RC walls and columns. Comput Struct 2018;196:246–62. https://doi.org/10.1016/j.compstruc.2017.10.010.

[42] Chang GA, Mander JB. Seismic energy based fatigue damage analysis of bridge columns: part I: evaluation of seismic capacity: NCEER Technical Report No. NCEER-94-0006 [RI. Buffalo, New York: the State University of New York; 1994.

[43] Areias P, Rabczuk T, Msekh MA. Phase-field analysis of finite-strain plates and shells including element subdivision. Comput Methods Appl Mech Eng 2016;312:322–50. https://doi.org/10.1016/j.cma.2016.01.020.

[44] Rabczuk T, Areias PMA, Belytschko T. A meshfree thin shell method for non-linear dynamic fracture. Int J Numer Methods Eng 2007;72:524–48. https://doi.org/10.1002/nme.2013.

[45] Markeset G, Hillerborg A. Softening of concrete in compression—localization and size effects. Cem Concr Res 1995;25:702–8.

[46] Bosco M, Ferrara E, Ghersi A, Marino EM, Rossi PP. Improvement of the model proposed by Menegotto and Pinto for steel. Eng Struct 2016;124:442–56.

https://doi.org/10.1016/j.engstruct.2016.06.037.

[47] Kunnath SK, Heo Y, Mohle JF. Nonlinear Uniaxial Material Model for Reinforcing Steel Bars. J Struct Eng 2009;135:335–43. https://doi.org/10.1061/(asce)0733-9445(2009)135:4(335).

[48] Filippou FC, Bertero VV, Popov EP. Effects of bond deterioration on hysteretic behavior of reinforced concrete joints 1983.

[49] Elmorsi M, Kianoush MR, Tso WK. Nonlinear analysis of cyclically loaded reinforced concrete structures. Struct J 1998;95:725–39.

[50] Marafi NA, Makdisi AJ, Eberhard MO, Berman JW. Impacts of an M9 Cascadia Subduction Zone Earthquake and Seattle Basin on Performance of RC Core Wall Buildings. J Struct Eng 2020;146:4019201.

[51] Bai Y, Lin X, Mou B. Numerical modeling on post-local buckling behavior of circular and square concrete-filled steel tubular beam columns. Int J Steel Struct 2016;16:531–46. https://doi.org/10.1007/s13296-016-6022-0.

[52] Akiyama H, Sekimoto H, Fukihara M, Nakanishi K, Hara K. A compression and shear loading tests of concrete filled steel bearing wall 1991.

[53] Haghi N, Epackachi S, Taghi Kazemi M. Macro modeling of steel-concrete composite shear walls. Structures 2020;23:383–406. https://doi.org/10.1016/j.istruc.2019.10.018.

[54] Coleman J, Spacone E. Localization Issues in Force-Based Frame Elements. J Struct Eng 2001;127:1257–65. https://doi.org/10.1061/(asce)0733-9445(2001)127:11(1257).

[55] Jansen DC, Shah SP. Effect of length on compressive strain softening of concrete. J Eng Mech 1997;123:25–35.

[56] Gupta RS. Pre-Stressed Concrete Structures. Princ. Struct. Des., vol. 18, 2019, p. 409–36. https://doi.org/10.1201/9781351027700-18.

[57] Mander JB, Priestley MJN, Park R. Theoretical stress-strain model for confined concrete. J Struct Eng 1988;114:1804–26.

[58] Cho SG, Park WK, So GH, Yi ST, Kim D. Seismic capacity estimation of Steel Plate Concrete (SC) shear wall specimens by nonlinear static analyses. KSCE J Civ Eng 2015;19:698–709. https://doi.org/10.1007/s12205-013-1271-3.

[59] Ma K, Ma Y, Liu B. Quasistatic Cyclic Tests and Finite Element Analysis of Low-Aspect Ratio Double Steel Concrete Composite Walls. Adv Civ Eng 2019;2019. https://doi.org/10.1155/2019/5917380.

[60] Epackachi S. Experimental, numerical, and analytical studies on the seismic response of steel-plate concrete (SC) composite shear walls. State University of New York at Buffalo; 2014.

[61] Epackachi S, Nguyen NH, Kurt EG, Whittaker AS, Varma AH. In-Plane Seismic Behavior of Rectangular Steel-Plate Composite Wall Piers. J Struct Eng 2015;141:04014176. https://doi.org/10.1061/(asce)st.1943-541x.0001148.

[62] Cheng C, Zhou D. Experimental study on seismic behavior of composite concrete and double-steel-plate shear walls with binding bars. Int. Conf. Adv. Exp. Struct. Eng., vol. 2015- Augus, University of Illinois Urbana-Champaign, United States; 2015.

[63] Nie JG, Hu HS, Fan JS, Tao MX, Li SY, Liu FJ. Experimental study on seismic behavior of high-strength concrete filled double-steel-plate composite walls. J Constr Steel Res 2013;88:206–19. https://doi.org/10.1016/j.jcsr.2013.05.001.

[64] Barkhordari MS, Tehranizadeh M, Scott MH. Numerical modelling strategy for predicting the response of reinforced concrete walls using Timoshenko theory. Mag Concr Res 2021;73:988–1010. https://doi.org/10.1680/jmacr.19.00542.

[65] Vu-Bac N, Lahmer T, Zhuang X, Nguyen-Thoi T, Rabczuk T. A software framework for probabilistic sensitivity analysis for computationally expensive models. Adv Eng Softw 2016;100:19–31. https://doi.org/10.1016/j.advengsoft.2016.06.005.

[66] Amini A, Abdollahi A, Hariri-Ardebili MA, Lall U. Copula-based reliability and sensitivity analysis of aging dams: Adaptive Kriging and polynomial chaos Kriging methods. Appl Soft Comput 2021;109:107524. https://doi.org/10.1016/j.asoc.2021.107524.